

Plasmon-Mediated Chiroptical Second Harmonic Generation from Seemingly Achiral Gold Nanorods

Zehua Li, Lei Kang,* Robert W. Lord, Kyoungweon Park, Andrew Gillman, Richard A. Vaia, Raymond E. Schaak, Douglas H. Werner, and Kenneth L. Knappenberger, Jr.*



Cite This: *ACS Nanosci. Au* 2022, 2, 32–39



Read Online

ACCESS |



Metrics & More



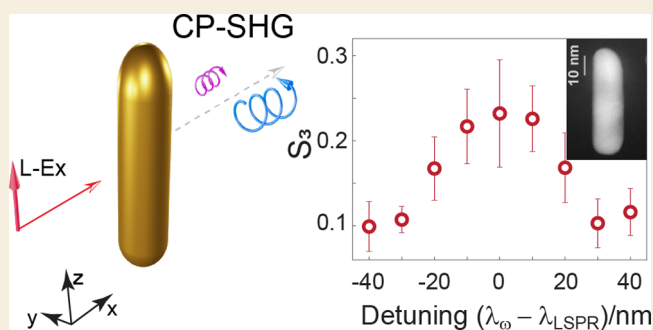
Article Recommendations



Supporting Information

ABSTRACT: Throughout nature, simple rules explain complex phenomena, such as the selective interaction of chiral objects with circularly polarized light. Here, we demonstrate chiroptical signals from gold nanorods, which are seemingly achiral structures. Shape anisotropy due to atomic-level faceting and rounding at the tips of nanorods, which are free of chiral surface ligands, induces linear-to-circular polarization modulation during second harmonic generation. The intrinsic nanorod chiroptical response is increased by plasmon-resonant excitation, which preferentially amplifies circularly polarized harmonic signals. This structure–plasmon interplay is uniquely resolved by polarization-resolved second harmonic generation measurements. The material's second-order polarizability is the product of the structure-dependent lattice-normal susceptibility and local surface plasmon field vectors. Synthetically scalable plasmon-supporting nanorods that amplify small circular dichroism signals provide a simple, assembly-free platform for chiroptical transduction.

KEYWORDS: gold nanoparticle, second harmonic generation, plasmon, chirality, nonlinearity



Chirality describes objects that change upon reflection, forming mirror image enantiomers that are not superimposable. Chiral objects are pervasive and determine function across many scientific disciplines including protein-making amino acids, anti-inflammatory drugs, chiral excitons and phonons in solid-state physics, topological superconductors, and polarization modulators in optical switches.^{1–7} Chiral enantiomers can have completely different functions, which necessitates their detection and separation. Light is the fastest way to identify and distinguish chiral objects. Therefore, the development of simple, sensitive chiroptical transducers is essential to trace-level molecular and virus sensing as well as to the development of efficient quantum and photonic circuits.

Circular dichroism (CD) signals, which result from the differential interaction with right and left circularly polarized light, are hallmarks of chiral objects. Though these signals are weak, they can be significantly amplified by plasmon-resonant excitation when metal nanoparticles are either assembled into chiral symmetries or are tethered to chiral molecules, such as proteins.^{5–14} For colloidal nanoparticle samples, linear CD effects have been attributed to the formation of geometrically chiral assemblies, as well as to interference between dipolar and higher-order modes. However, strain-induced shape anisotropies^{15,16} are thought to play key roles in inducing CD in second harmonic generation (SHG) signals of nanoparticle dimers.⁴ Circular dichroism has been detected in the nonlinear

optical (NLO) response of lithographically formed chiral structures, and metal waveguides have also been used to increase Raman optical activity signals of chiral molecules.^{17–23} Regardless of the CD mechanism, all of these examples require the use of complex metal structures that are not easily scalable. Here, we report CD-SHG for a simple and scalable achiral object—a single gold nanorod—and link the chiroptical response to atomic-level lattice properties and resonant surface fields. This approach can greatly simplify the design of plasmon-based CD transduction.

LATTICE ANISOTROPY LEADS TO NONLINEAR CHIROPTICAL RESPONSES

Isolated, nonaggregated, colloidal metal nanorods provide opportunities to modulate the amplitude and polarization of SHG signals because plasmon-mediated NLO responses are determined by both resonant field enhancements and the microscopic (and macroscopic) polarizabilities of the materi-

Received: July 14, 2021

Published: September 21, 2021



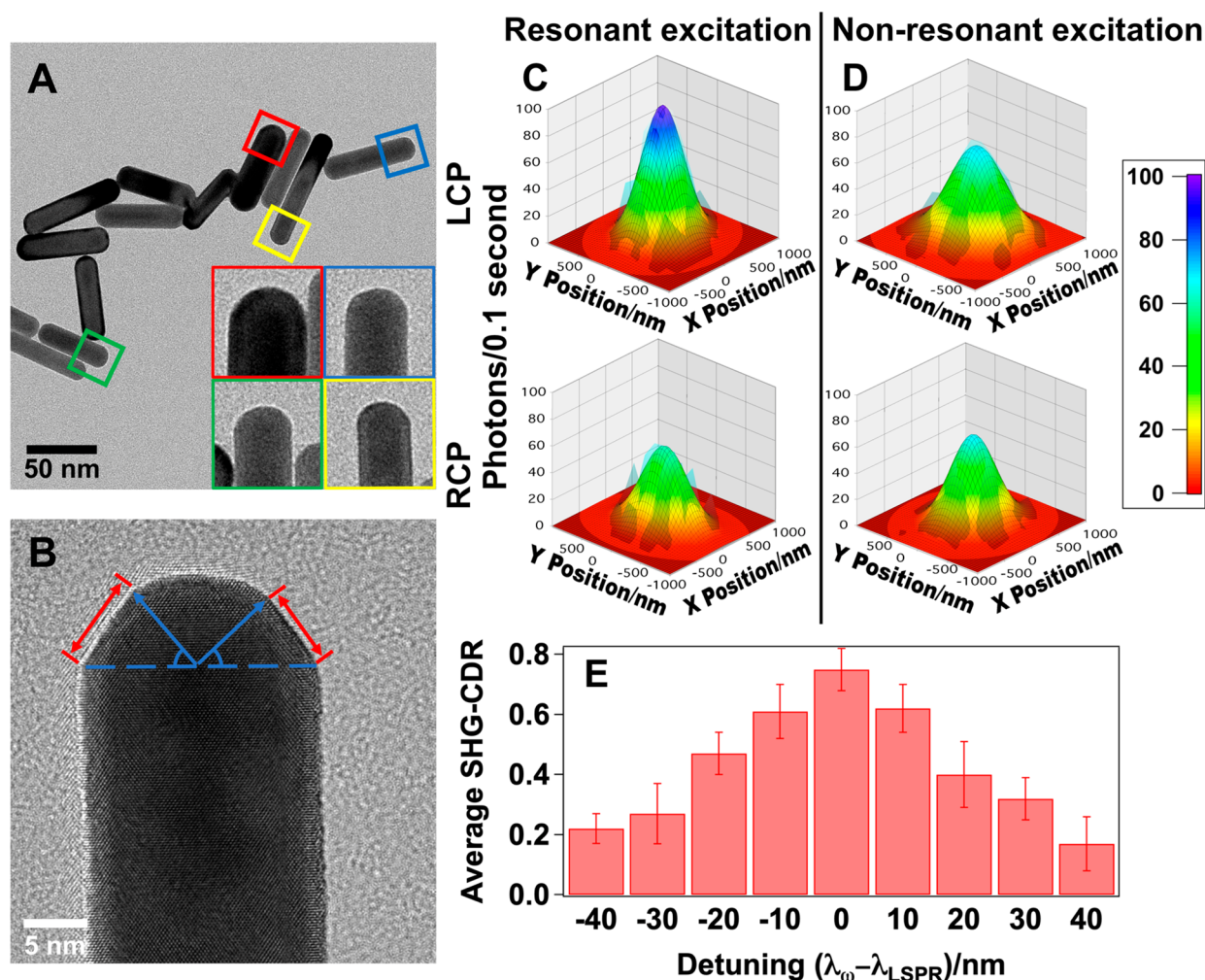


Figure 1. Characterization of gold nanorod shape anisotropy and chiroptical signals. (A) Transmission electron microscopy (TEM) imaging survey of multiple nanorods showing particle-to-particle variations in tip anisotropy (inset). (B) High-resolution TEM image of one nanorod tip. The tip anisotropy is depicted by the double-sided red arrows and the distinctly different bisecting angles (blue). (C,D) Schematic of raw second harmonic generation (SHG) data with an overlay of 3-D Gaussian point spread functions obtained from a single nanorod when the left (top) and right (bottom) circularly polarized laser pulses are resonant (C) and nonresonant (D) with the 800 nm longitudinal surface plasmon resonance of the particle. The resonant (C) and nonresonant (D) data were obtained using fundamental wavelengths of 800 and 690 nm, respectively. The data in (D) produce a circular dichroism ratio (CDR) value of 0.28 ± 0.05 , reflecting the intrinsic chiroptical response of the asymmetric nanorod. Plasmon-resonant excitation (C) increased the CDR value to 0.67 ± 0.08 . Mean and standard deviations of SHG-detected CDRs (described in main text) obtained for a single nanorod by tuning the wavelength from 760 to 840 nm. The number of photons used for calculating the CDR value was determined to $2\text{-}\sigma$ confidence (Materials and Methods in the Supporting Information). The data plotted in panel (E) reflect the mean and standard deviations from repeating measurements at each wavelength in triplicate.

al.²⁴ Differences in lattice parameters due to twinning, strain, and overall shape anisotropies contribute to the material's microscopic nonlinear susceptibility. Indeed, changes in metal-metal atom bond lengths on the subangstrom scale are known to induce large second-order responses in 2-D metals.²⁵ Most commonly, gold nanorods are formed in solution by silver-ion-assisted, seed-mediated synthesis that utilizes cationic surfactants, such as cetyltrimethylammonium bromide (CTAB).^{26–28} Although this approach typically yields single-crystalline nanorods, the final structures are characterized by rounded or faceted tips and an overall asymmetric shape when viewed at the atomic level.¹⁶ Scanning transmission electron microscopy (STEM) images of several gold nanorods used in this study are shown in Figures 1A and S1A. These images reflect the rounding effect apparent on many different particles, and Figure 1B depicts the anisotropy for one of the nanorods. The blue lines in Figure 1B denote a

difference in length of approximately 25%, due to asymmetry at the tips of the nanorods. This anisotropy results from the nanorod longitudinal growth mechanism, which induces metal lattice strain and surface reconstruction.^{29,30} The anisotropy was quantified using an asymmetry metric (AS), calculated from Frechet parameters determined from STEM imaging (Figures S1–S4). The AS for the nanorods was 0.033 (Figure S1B); the AS value for perfectly symmetric rods would be 0. The asymmetry metric decreases $\sim 20\%$ from 0.33 to 0.027 as the gold nanorods are reshaped to a more thermally stable morphology. The asymmetry quantified by the AS value provides the structural mirror symmetry breaking needed to induce second harmonic generation and chiroptical signals.

CD arising from the intrinsic asymmetry of the nanorods may be further enhanced by plasmon-resonant SHG. Excitation of the longitudinal surface plasmon resonance (LSPR) generates surface fields with significant polarizability

contributions oriented perpendicular to the nanorod surface and coaligned with the fundamental and harmonic wave vectors. This type of projection should amplify the intrinsic chiroptical signals expected from the anisotropic nanorods. Hence, structural effects at the atomic level of the gold nanorod lattice may lead to plasmon-mediated polarization modulation of NLO signals that can be observed in the far-field.

To determine if local symmetry breaking leads to chiroptical signals for achiral nanorods, we measured LSPR-mediated second harmonic generation, including linear to circular polarization modulations, for isolated gold nanorods. First, the second harmonic response measured from single gold nanorods (Figure S5) is evaluated using circularly polarized fundamental laser pulses (Figure 1C,D and Figures S6 and S7). Figure 1C compares the three-dimensional Gaussian point spread functions obtained when a single nanorod is excited using laser pulses that are either resonant (Figure 1C; 800 nm) or nonresonant (Figure 1D; 690 nm) with the particle longitudinal surface plasmon mode. Figure 1C portrays the large differences in detected second harmonic intensities when left (Figure 1C, top) and right (Figure 1C, bottom) circularly polarized fundamental light is used for plasmon-resonant SHG. In contrast, similar SHG intensities resulted from left (Figure 1D, top) and right (Figure 1D, bottom) circularly polarized fundamental under nonresonant conditions. The CD responses were quantified using the CD ratio, $\text{SHG-CDR} = |2(I_{2\omega}^{\text{LCP}} - I_{2\omega}^{\text{RCP}})/(I_{2\omega}^{\text{LCP}} + I_{2\omega}^{\text{RCP}})|$, where $I_{2\omega}^{\text{LCP}}$ and $I_{2\omega}^{\text{RCP}}$ represent the intensity of second harmonic signals resulting from left and right circularly polarized fundamental light, respectively.⁸ This analysis yielded CDR ratios of 0.67 ± 0.08 and 0.28 ± 0.05 for the single-particle measurements shown in Figure 1C and 1D, respectively. These data implicate resonance matching with the longitudinal plasmon mode for intensifying the intrinsic nanorod CD response. We note that this effect was general in these studies and confirmed both by scanning the fundamental wavelength to determine wavelength-dependent CDR values as well as by surveying nanorods of different aspect ratios while using a fixed fundamental wavelength of 800 nm. The results from the former case are summarized in Figure 1E, which exhibits increased CDR as the difference between the LSPR and fundamental wavelengths approached zero. CDR values decreased for fundamental detuning to both longer and shorter wavelengths. This trend was also observed when single-nanorod SHG-CDR measurements were made on a large number of nanorods using a fixed 800 nm fundamental (Figure S7). In addition to the significance of plasmon resonance matching, Figure S7 also shows the structural specificity of the response as both positive and negative SHG-CDR polarities were measured, which reflects the existence of both right and left handed enantiomers.

■ PLASMON-RESONANT EXCITATION SELECTIVELY AMPLIFIES CIRCULARLY POLARIZED SECOND HARMONIC SIGNALS FOR GOLD NANORODS

Next, plasmon-mediated linear-to-circular polarization modulation by the nanorods was investigated. The modulation effect was analyzed by determining SHG Stokes parameters over a broad tuning range of the laser fundamental, as described in the Supporting Information (Figure S8).³¹ The total Stokes vector, S , describes the polarization of the second harmonic field using four components, S_0 , S_1 , S_2 , and S_3 . The Stokes parameters can be determined by quantifying the second

harmonic intensity, $I_{2\omega}$, as functions of the light polarization (θ) and phase (ϕ) as

$$I_{2\omega}(\theta, \phi) = \frac{1}{2}(S_0 + S_1 \cos 2\theta + S_2 \cos \phi \sin 2\theta + S_3 \sin \phi \sin 2\theta) \quad (1)$$

where S_0 is the total harmonic intensity, S_1 is the contribution from light linearly polarized along the nanorod axis (formally the intensity difference of linearly polarized harmonic signals emitted parallel and perpendicular to the nanorod longitudinal axis), S_2 is the intensity difference between linearly polarized components emitted at $\pm 45^\circ$ with respect to the longitudinal axis, and S_3 describes the intensity difference from left and right circularly polarized harmonic light generated by orienting the linearly polarized fundamental parallel to the nanorod longitudinal axis.

Figure 2 summarizes the effects of resonance matching between fundamental and nanorod LSPR wavelengths on the SHG Stokes signals, which is important for understanding the selective plasmon amplification of specific polarization states. The dark-field scattering spectrum from one nanorod is shown in Figure 2A (top), along with a Lorentzian fit to the peak. Figure 2A (bottom) summarizes the wavelength-dependent Stokes parameters for the same nanorod. This comparison shows a clear decrease in linearly polarized SHG, S_1 (red), when the fundamental resonance is matched to the LSPR wavelength. The S_2 component (black) was independent of the fundamental wavelength. An increase in circularly polarized SHG, S_3 (blue), which complemented the S_1 decrease, was observed upon resonance matching. Figure 2A data reflect an increased contribution from circularly polarized harmonic generation upon plasmon resonance matching with the laser fundamental. Although, Figure 2 data portray the response from a single nanorod, the observation of an increased degree of circular polarization in harmonic generation was generalizable to a large survey of more than 50 single-nanorod measurements. This response was observed both by changing the fundamental wavelength used for a single nanorod and by tuning the LSPR for fixed fundamental wavelengths ($\lambda_\omega = 800$ nm) through variation of the nanorod length-to-diameter aspect ratio. Furthermore, we note that S_3 responses corresponding to both left- and right-handed nanorods were obtained (Figure 2B), reflecting the structure sensitivity of the measurement. In order to ensure the Stokes parameters summarized in Figure 2 resulted from the nanorod response, the measurements were repeated on a thin beta-barium borate (β -BBO) reference crystal placed at the microscope sample-focus plane. The reference crystal is not expected to have a wavelength-dependent response over the range studied. The wavelength-dependent S_3 values from the reference are compared to the nanorod in Figure 2A (green); S_1 , S_2 , and S_3 are summarized in Figure S8. The β -BBO Stokes parameters were invariant with wavelength, and the S_1 parameter contributed more than 90% of the SHG response; S_2 and S_3 equated to less than 3% of the signal and represent the polarization sensitivity limit of the measurement. Hence, the off-resonant nanorod S_3 value of 10% can be attributed to the intrinsic CD response of the nanorod, which was increased by approximately $3\times$ (30%) upon fundamental LSPR matching. The results validate that plasmon-resonant excitation increases the CD response of an object.

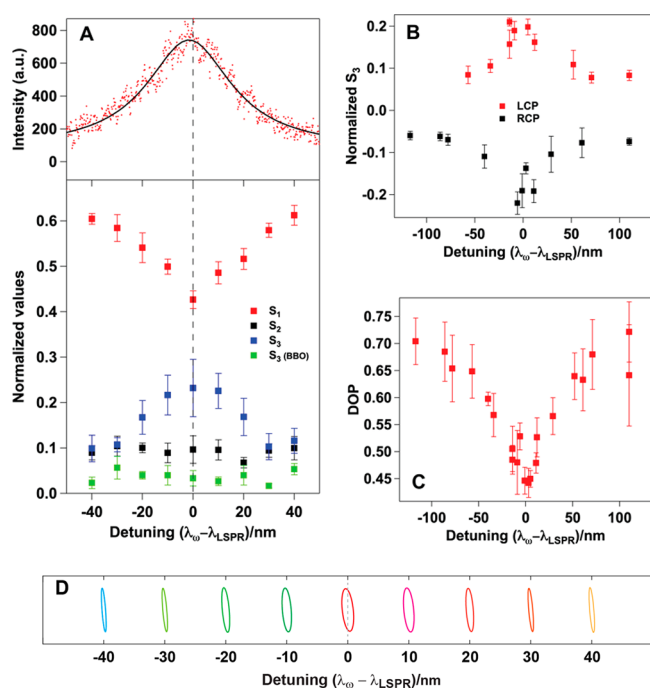


Figure 2. Plasmon-mediated gold nanorod SHG. (A) (Top) Dark-field scattering spectrum overlaid with the Lorentzian fit for a single nanorod analyzed in this study. (Bottom) Comparison of resonance spectrum (top) and SHG Stokes parameters of S_1 (red), S_2 (black), and S_3 (blue) for a single nanorod measured using several fundamental wavelengths, including plasmon-resonant and detuning excitations that spanned ± 40 nm. The absolute values of S_1 , S_2 , and S_3 are normalized to S_0 . The error bars represent the standard deviations of three identical measurements. The increased S_3 obtained upon resonance matching of the fundamental and nanorod LSPR indicates a larger contribution of circular polarization, which agrees well with CDR data shown in Figure 1C–E. The green data are obtained from an achiral reference, β -BBO, and represent the S_3 sensitivity of the measurement. (B) Wavelength-dependent positive (red) and negative (black) S_3 values and degrees of polarization (C) calculated by $DOP = \sqrt{S_1^2 + S_2^2 + S_3^2} / S_0$ for over 20 single nanorods with LSPR ranging from 670 to 930 nm ($\lambda_{\omega} = 800$ nm). The average and standard deviations reported are obtained from the statistical analysis of measurements performed in triplicate. Each individual measurement is made at the $2\text{-}\sigma$ confidence level. The nonzero values across the range indicate a superposition of linear and circular polarization. The largest circular contribution is observed for fundamental LSPR matching. (D) Polarization ellipses rendered from experimentally determined Stokes parameters. The trend in the ellipses shows the dominance of the linear polarization state in the harmonic signal when the laser fundamental is detuned from the LSPR and the increased contribution from the circular state when the nanorod is resonantly excited.

The Stokes parameters were also analyzed to determine the purity, or degree of polarization, of the harmonic field. For pure light polarization states, either linear or circular, $S_0^2 = S_1^2 + S_2^2 + S_3^2$, whereas mixed polarization states yield $S_0^2 > S_1^2 + S_2^2 + S_3^2$.²⁷ Hence, a nonzero difference between S_0^2 and the summation over the remaining Stokes parameters indicates the harmonic wave is a superposition of polarization states. The resultant degree of polarization, DOP, for the harmonic signal is calculated as $DOP = \sqrt{S_1^2 + S_2^2 + S_3^2} / S_0$. The degree of polarization obtained from a survey of nanorods is plotted in Figure 2C. Similar to the S_1 and S_3 trends, the degree of

polarization values depended on LSPR matching with the fundamental ($\lambda_{\omega} = 800$ nm), with the smallest DOP ($\approx 45\%$) occurring for the resonant cases. Based on these observations, it was apparent that a pure harmonic polarization state was not observed at any wavelength. Rather, the harmonic signal was a superposition of linear and circular polarization states. Further, because the difference was largest for resonant conditions, plasmon excitation leads to a larger increase in the circular contribution to the harmonic frequency. In the case of harmonic generation without LSPR excitation, the harmonic wave is dominated by linear polarization states, although contributions from circular components are nonzero (i.e., $DOP \approx 70\%$). The implication of the Figure 2C data is two-fold: (i) even off-resonant SHG transduced by the nanorods included circular dichroism, and (ii) plasmon-resonant excitation preferentially increases the intrinsic linear-to-circular transduction over the linear-to-linear process. These effects are illustrated in Figure 2D, which shows the resultant harmonic polarization ellipses for various fundamental LSPR matching conditions. For the off-resonant case (e.g., $\Delta\lambda = \pm 40$ nm), the signal is dominated by a linear, vertical polarization state. However, for zero detuning, the horizontal contribution to the ellipse becomes prominent, reflecting the increased circularly polarized contribution to the harmonic signal. Hence, plasmon-resonant excitation selectively amplifies the CD response of the asymmetric nanorod.

To determine the importance of local structure on plasmon-mediated CD, we studied symmetric nanorods formed by thermal reshaping of the original asymmetric structures (Figures S1 and S4).³² The AS for the reshaped rods was $\sim 20\%$ lower than that for the original sample. The SHG yield from reshaped nanorods was too low to reliably quantify polarization metrics, confirming the interpretation that subtle symmetry breaking induces intrinsic CD-SHG, which can be amplified by plasmon-resonant excitation.

Chiroptical responses for isolated and aggregated nanorods have been studied using linear methods.^{11–14} Significant circular dichroism dark-field scattering (CD-DFS) signals are obtained for protein-assembled dimers and higher-order multimers of gold nanorods.^{12–14} The strong CD is attributed to the ability to form chiral assemblies and to electronic coupling between plasmon modes and excitations of the protein. However, despite lattice properties that enable isolated gold nanoparticles to exhibit nonlinear chiroptical signatures, single-particle CD-DFS measurements on both nanorods and nanodumbbells do not yield responses detectable above noise.^{13,14} Polarization-resolved SHG is more sensitive to the chiroptical signals originating from isolated nanoparticles than linear scattering. This can be understood by considering the Lorentz reciprocity theorem,²⁴ which describes the electric field, ($E_{nl}(2\omega)$), of SHG photons detected experimentally in the far-field:

$$E_{nl}(2\omega) \propto \iint \chi_{nnn}^{(2)} E_n^2(\omega) \cdot E_n(2\omega) dS \quad (2)$$

where χ_{nnn} is the surface-normal nonlinear susceptibility, $E_n(\omega)$ and $E_n(2\omega)$ are the local field amplitudes normal to the nanostructure's interface at the fundamental and second harmonic frequencies, respectively. Equation 2 makes clear that the harmonic signal is the product of the lattice-dependent susceptibility tensor and the fundamental and harmonic surface fields. Hence, structural influences on optical signals are

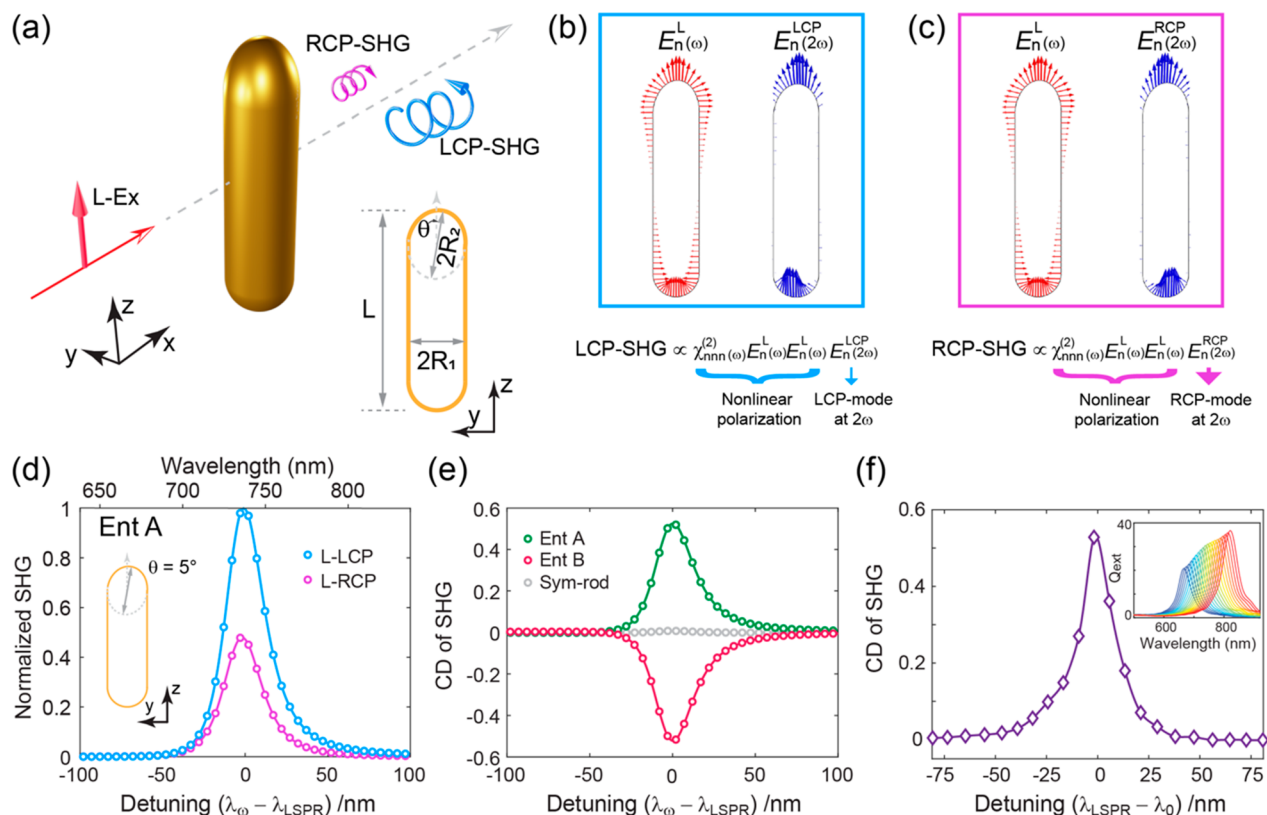


Figure 3. Circularly polarized SHG predicted by nonlinear scattering theory. (A) Schematic of SHG dichroism from an asymmetric gold nanorod illuminated by a linearly polarized fundamental wave. The nanorod is embedded in a background with permittivity 1. Geometrical parameters: $R_1 = 7$ nm, $R_2 = 10$ nm, $L = 34.5$ nm, and $\theta = 5^\circ$ (enantiomer A). (B) Vector distribution of simulated electric field normal to the surface of the nanorod (Ent A) on the $x = 0$ nm plane. Left: Under illumination of a linearly polarized wave at the fundamental wavelength (740 nm). Right: LCP mode at second harmonic wavelength (370 nm). (C) Same field plot as in (B) but for RCP mode at 370 nm on the right. (D) Calculated circularly polarized SHG signal emitted from the nanorod (Ent A) under a linear polarization excitation. The results are normalized to the maximum value of L-LCP. (E) Corresponding circular dichroism (CD = L-LCP - L-RCP) of the SHG signal emitted from both enantiomers. Results of an ideally symmetric rod ($\theta = 0^\circ$) is also presented. (F) Dependence of circularly polarized SHG on the plasmon resonance of an asymmetric gold nanorod (Ent A). In simulations, a linear polarization at a fixed fundamental wavelength ($\lambda_0 = 740$ nm) is used to excite the nanorod with a range of length-to-radius aspect ratios ($AR = L/2R_1$). Inset: Corresponding normalized extinction cross section (Q_{ext}) spectra.

amplified for second-order nonlinear measurements, as compared to linear ones.

■ NANOROD TIP ASYMMETRY MEDIATES THE LINEAR-TO-CIRCULAR POLARIZATION MODULATION

Next, the experimental second harmonic results are compared to numerical simulations. Without loss of generality, the asymmetry of the gold nanorod conveyed by TEM images (Figure 1A,B and Figure S1–S4) is introduced in our numerical study by a semiellipsoid tip whose major axis is slightly rotated with respect to the growth axis of the nanorod (Figure 3A). This is accomplished using a major axis rotation (θ) of the semiellipsoid tip in the $x = 0$ nm plane, which is perpendicular to the propagation direction of the linearly polarized incident light (Figure 3A). Accordingly, we define the nanorod with θ of positive (negative) rotations as enantiomer A (B). In order to understand the origin of the observed circularly polarized SHG emission from the isolated gold nanorods, we perform scattering simulations and calculate the SHG based on nonlinear scattering theory, which has recently been used to accurately predict frequency doubling in plasmonic nanostructures.³³ In particular, the electric field of SHG in the far-field region ($E_{\text{nl}}(2\omega)$) can be analyzed using eq

2.²⁴ Employing this method, Chen and co-workers have calculated the polarization-dependent SHG from Trisceli-type plasmonic nanostructures, showing a good agreement with experimental measurements.²¹

To assess the circularly polarized SHG from plasmonic nanostructures, polarity-dependent field distributions at the nonlinear frequency ($E_{\text{n}}^{\text{CP}}(2\omega)$) are used to describe the propagation of the radiation induced by the nonlinear polarization $P^{\text{NL}} \propto \chi_{\text{nnn}} E_{\text{n}}^2(\omega)$.²² The vector distribution (on $x = 0$ nm plane) of $E_{\text{n}}^{\text{L}}(\omega)$ is illustrated in Figure 3B (left), corresponding to the nanorod under excitation with a linearly (z -) polarized wave at the longitudinal plasmon resonance (fundamental, $\lambda_\omega = \lambda_{\text{LSPR}} = 740$ nm) frequency, whereas that of $E_{\text{n}}^{\text{LCP}}(2\omega)$ (Figure 3B (right)) denotes the LCP mode of the structure at the second harmonic frequency. The SHG for L-LCP (linear fundamental to left circularly polarized harmonic) in the far-field region is determined by the overlap integral between $\chi_{\text{nnn}} E_{\text{n}}^{\text{L}}(\omega) E_{\text{n}}^{\text{L}}(\omega)$ and $E_{\text{n}}^{\text{LCP}}(2\omega)$ on the surface of the nanorod. L-RCP SHG results from the contribution of $\chi_{\text{nnn}} E_{\text{n}}^{\text{L}}(\omega) E_{\text{n}}^{\text{L}}(\omega)$ and $E_{\text{n}}^{\text{RCP}}(2\omega)$, in which the latter is the RCP mode at 2ω , as depicted in Figure 3C. In Figure 3D, we present the simulated SHG spectra of both LCP and RCP components for enantiomer A. It is found that SHG for L-LCP at wavelengths around λ_{LSPR} is significantly larger than that for

L-RCP. In sharp contrast, as shown in Figure S9A,B, enantiomer B exhibits a polarity-inverted, circularly polarized second harmonic response. The CD spectra of SHG emission from both enantiomers are shown in Figure 3E, which clearly reveals the interplay between nanorod structure and plasmon-resonant excitation for the generation of circularly polarized SHG; the enantiomeric specificity is captured by the simulations. Providing a qualitative S_3 comparison, the simulated CD-SHG emission spectra indicate good agreement with the measured wavelength-dependent trends shown in Figure 2. The wavelength-independent near-zero CD spectrum of an ideal symmetric nanorod (Figure 3E; $\theta = 0^\circ$) verifies the accuracy of the simulation method.

To better illustrate the underlying physics of the observed polarity-dependent SHG-CD at the LSPR, we perform field analysis for enantiomer A and present the results in Figure S10. The simulated field map of $E_n^L(\omega)$ on the $x = 0$ nm plane (Figure S10B) reveals an asymmetric field distribution, which can be clearly seen in the plots truncated to the nanorod tip regions of $|E_n^L(\omega)|$ and y -component phase of the field, that is, $\arg(E_n^{L,y}(\omega))$. Furthermore, close inspection of the distributions of $|E_n^{L,CP}(2\omega)|$ and $|E_n^{R,CP}(2\omega)|$ (Figure S10C) shows that the harmonic LCP mode at 2ω has a stronger surface field at the two nanorod tips. The generation of asymmetric field responses at both fundamental and second harmonic frequencies are the dominant sources that mediate circularly polarized SHG emission. To better visualize the nonlinear contribution, that is, the integrand of eq 2, the amplitude (top row) and phase (bottom row) distributions of $E_n^L(\omega)E_n^L(\omega)E_n^{CP}(2\omega)$ on different cross sections are shown in Figure S10D–I. Only contributions at the gold/medium interface have been evaluated. The amplitude plots clearly show that the dominant contribution to both L-LCP and L-RCP SHG originates from the areas associated with the two tips of the nanorods. Figure S10D,G portrays the distinct localization and phase distribution associated with the handedness, or polarity, of LCP and RCP modes at 2ω that were induced using linearly polarized fundamental. This is made evident by Figure S10F, which unambiguously illustrates a stronger contribution around the upper nanorod tip for L-LCP than for L-RCP. In particular, the maximum value of $|E_n^L(\omega)E_n^L(\omega)E_n^{L,CP}(2\omega)|$ is 14% larger than that of $|E_n^L(\omega)E_n^L(\omega)E_n^{R,CP}(2\omega)|$, while the corresponding integral (in the $z = 30$ nm plane) for L-LCP is 23% greater than that for L-RCP. Note that, as expected, identical amplitude and phase distributions are observed in the $x = 0$ nm cutting plane (Figure S10E,H) due to the symmetry of the structure. These results further validate that the structural asymmetry at the nanorod tips provides a chiroptical signal source, which leads to the nanoparticle-specific circular dichroism detected in the second harmonic signals. The longitudinal plasmon resonance significantly increases the nonlinearity to enable unambiguous CD-SHG detection in the far-field.

By varying the aspect ratio (AR) of the enantiomer A, we further study CD-SHG as a function of the plasmonic resonance detuning of the gold nanorods. The simulated extinction cross section spectra shown in Figure S11A and Figure 3F inset indicate a red shift of the plasmonic resonance of the nanorod from ~ 660 to 820 nm with increasing AR in a range from 3.5 to 5.5. To simulate the resonance detuning effect, a z -polarized fundamental wave at a fixed wavelength (λ_0) of 740 nm is used to excite the nanorods. Figure S11B summarizes the dependence of L-LCP and L-RCP SHG on the

resonance detuning $\Delta\lambda = \lambda_{\text{res}} - \lambda_0$, whereas Figure 3F shows the corresponding CD of SHG, indicating the close dependence of the chiroptical nonlinearity on plasmon-resonant excitation. Results shown in Figure 3 and Figure S11 agree with the experimental observations in Figure 2.

CONCLUSIONS

Here, the nonlinear chiroptical responses of an isolated achiral object—a CTAB-protected gold nanorod—are described. The complete second harmonic generation signal is a superposition of linear and circular polarization states. Using a combination of polarization-resolved single-nanoparticle SHG imaging, electron microscopy, and numerical modeling, we show that the circular dichroism second harmonic is due to shape anisotropy at the nanorod tips. As a result, the circularly polarized contribution to the NLO superposition increases when the fundamental wave resonantly excites longitudinal plasmon modes of the nanorod, inducing asymmetric surface fields localized at the tips and spatially colocalized with the particle anisotropy. Because the SHG signal is a product of the structure-dependent microscopic polarizability and local surface fields, these measurements more sensitively probe the chiroptical responses of metal nanoparticles and more accurately determine the contributions from material structure and plasmon amplification than is possible using linear methods. The findings provide new insights into nanoparticle-based circular dichroism, showing that the intrinsic metal lattice structure must be considered. These conclusions pave the way for developing nanoparticle-based chiroptical transducers by leveraging atomic-level structure. Amplification of CD signals using isolated particles, in place of assemblies that require specific nanoparticle-to-nanoparticle orientations to achieve similar effects, will greatly simplify the scalability and robustness of chiroptical sensors. In addition, silver nanorods are formed with shape anisotropies similar to those shown here and can be expected to show similar chiroptical responses but at material-specific wavelengths.³⁴ Hence, expanding metal composition, size, and shape could provide a straightforward route to broadly tunable chiroptical materials. Such advances could allow for trace-level molecular, protein, and virus sensing, as well as polarization modulation in photonic circuits.

ASSOCIATED CONTENT

Supporting Information

The Supporting Information is available free of charge at <https://pubs.acs.org/doi/10.1021/acsnanoscienceau.1c00014>.

Description of experimental and computational methods, analysis of nanorod asymmetric metrics, supplemental Figures S1–S11 depicting SHG spectra, Stokes parameters, electron micrographs, and simulated nanorod extinction spectra (PDF)

AUTHOR INFORMATION

Corresponding Authors

Kenneth L. Knappenberger, Jr. — Department of Chemistry, The Pennsylvania State University, University Park, Pennsylvania 16802, United States; orcid.org/0000-0003-4123-3663; Email: klk260@psu.edu

Lei Kang — Department of Electrical Engineering and Center for Nanoscale Science, The Pennsylvania State University,

University Park, Pennsylvania 16802, United States;
orcid.org/0000-0001-7718-7756; Email: lzk12@psu.edu

Authors

Zehua Li – Department of Chemistry, The Pennsylvania State University, University Park, Pennsylvania 16802, United States

Robert W. Lord – Department of Chemistry, The Pennsylvania State University, University Park, Pennsylvania 16802, United States; orcid.org/0000-0003-1487-1598

Kyoungweon Park – Air Force Research Laboratory, Wright-Patterson Air Force Base, Ohio 45433, United States; orcid.org/0000-0001-8069-3000

Andrew Gillman – Air Force Research Laboratory, Wright-Patterson Air Force Base, Ohio 45433, United States

Richard A. Vaia – Air Force Research Laboratory, Wright-Patterson Air Force Base, Ohio 45433, United States; orcid.org/0000-0003-4589-3423

Raymond E. Schaak – Department of Chemistry, The Pennsylvania State University, University Park, Pennsylvania 16802, United States; Department of Chemical Engineering, The Pennsylvania State University, University Park, Pennsylvania 16802, United States; orcid.org/0000-0002-7468-8181

Douglas H. Werner – Department of Electrical Engineering and Center for Nanoscale Science, The Pennsylvania State University, University Park, Pennsylvania 16802, United States

Complete contact information is available at:

<https://pubs.acs.org/10.1021/acsnanoscienceau.1c00014>

Author Contributions

Z.L. performed nonlinear optical measurements and analysis under the supervision of K.L.K. K.P., A.G., and R.A.V. synthesized the nanoparticles and performed electron tomography measurements and statistical analysis. L.K. performed numerical simulations. R.L. performed electron microscopy under the supervision of R.E.S. L.K. and K.L.K. wrote the manuscript with input from all other authors.

Notes

The authors declare no competing financial interest.

ACKNOWLEDGMENTS

This research was supported by the Air Force Office of Scientific Research, Grant No. FA-9550-18-1-0347. This work was also supported by National Science Foundation, Award Nos. CHE-1807999 and CHE-1707830. Partial support for this work was also provided by the John L. and Genevieve H. McCain endowed chair professorship at the Pennsylvania State University.

REFERENCES

- (1) Ben-Moshe, A.; da Silva, A.; Muller, A.; Abu-Odeh, A.; Harrison, P.; Waelder, J.; Niroui, F.; Ophus, C.; Minor, A. M.; Asta, M.; Theis, W.; Ercius, P.; Alivisatos, A. P. The Chain of Chirality Transfer in Tellurium Nanocrystals. *Science* **2021**, *372*, 729–733.
- (2) Agranat, I.; Caner, H.; Caldwell, J. Putting Chirality to Work: The Strategy of Chiral Switches. *Nat. Rev. Drug Discovery* **2002**, *1*, 753–768.
- (3) Yang, Y.; da Costa, R. C.; Fuchter, M. J.; Campbell, A. J. Circularly Polarized Light Detection by a Chiral Organic Semiconductor Transistor. *Nat. Photonics* **2013**, *7*, 634–638.

- (4) Qi, X.-L.; Hughes, T. L.; Zhang, S.-C. Chiral Topological Superconductor from the Quantum Hall State. *Phys. Rev. B: Condens. Matter Mater. Phys.* **2010**, *82*, 184516.

- (5) Kuzyk, A.; Schreiber, R.; Fan, Z.; Pardatscher, G.; Roller, E.-M.; Högele, A.; Simmel, F. C.; Govorov, A. O.; Liedl, T. DNA-Based Self-Assembly of Chiral Plasmonic Nanostructures with Tailored Optical Response. *Nature* **2012**, *483*, 311–314.

- (6) Govorov, A. O.; Fan, Z.; Hernandez, P.; Slocik, J. M.; Naik, R. R. Theory of Circular Dichroism of Nanomaterials Comprising Chiral Molecules and Nanocrystals: Plasmon Enhancement, Dipole Interactions, and Dielectric Effects. *Nano Lett.* **2010**, *10*, 1374–1382.

- (7) Fan, Z.; Govorov, A. O. Plasmonic Circular Dichroism of Chiral Metal Nanoparticle Assemblies. *Nano Lett.* **2010**, *10*, 2580–2587.

- (8) Chandra, M.; Dowgiallo, A.-M.; Knappenberger, K. L. Magnetic Dipolar Interactions in Solid Gold Nanosphere Dimers. *J. Am. Chem. Soc.* **2012**, *134*, 4477–4480.

- (9) Ma, W.; Xu, L.; de Moura, A. F.; Wu, X.; Kuang, H.; Xu, C.; Kotov, N. A. Chiral Inorganic Nanostructures. *Chem. Rev.* **2017**, *117*, 8041–8093.

- (10) Famularo, N. R.; Kang, L.; Li, Z.; Zhao, T.; Knappenberger, K. L.; Keating, C. D.; Werner, D. H. Linear and Nonlinear Chiroptical Response from Individual 3D Printed Plasmonic and Dielectric Micro-Helices. *J. Chem. Phys.* **2020**, *153*, 154702.

- (11) Spaeth, P.; Adhikari, S.; Le, L.; Jollans, T.; Pud, S.; Albrecht, W.; Bauer, T.; Caldarella, M.; Kuipers, L.; Orrit, M. Circular Dichroism Measurement of Single Metal Nanoparticles Using Photothermal Imaging. *Nano Lett.* **2019**, *19*, 8934–8940.

- (12) Wang, L.-Y.; Smith, K. W.; Dominguez-Medina, S.; Moody, N.; Olson, J. M.; Zhang, H.; Chang, W.-S.; Kotov, N.; Link, S. Circular Differential Scattering of Single Chiral Self-Assembled Gold Nanorod Dimers. *ACS Photonics* **2015**, *2*, 1602–1610.

- (13) Smith, K. W.; Zhao, H.; Zhang, H.; Sánchez-Iglesias, A.; Grzelczak, M.; Wang, Y.; Chang, W.-S.; Nordlander, P.; Liz-Marzán, L. M.; Link, S. Chiral and Achiral Nanodumbbell Dimers: The Effect of Geometry on Plasmonic Properties. *ACS Nano* **2016**, *10*, 6180–6188.

- (14) Zhang, Q.; Hernandez, T.; Smith, K. W.; Hosseini Jebeli, S. A.; Dai, A. X.; Warning, L.; Baiyasi, R.; McCarthy, L. A.; Guo, H.; Chen, D.-H.; Dionne, J. A.; Landes, C. F.; Link, S. Unraveling the Origin of Chirality from Plasmonic Nanoparticle-Protein Complexes. *Science* **2019**, *365*, 1475–1478.

- (15) Johnson, C. L.; Snoeck, E.; Ezcurdia, M.; Rodríguez-González, B.; Pastoriza-Santos, I.; Liz-Marzán, L. M.; Hÿtch, M. J. Effects of Elastic Anisotropy on Strain Distributions in Decahedral Gold Nanoparticles. *Nat. Mater.* **2008**, *7*, 120–124.

- (16) Walsh, M. J.; Barrow, S. J.; Tong, W.; Funston, A. M.; Etheridge, J. Symmetry Breaking and Silver in Gold Nanorod Growth. *ACS Nano* **2015**, *9*, 715–724.

- (17) Walter, F.; Li, G.; Meier, C.; Zhang, S.; Zentgraf, T. Ultrathin Nonlinear Metasurface for Optical Image Encoding. *Nano Lett.* **2017**, *17*, 3171–3175.

- (18) Li, G.; Zhang, S.; Zentgraf, T. Nonlinear Photonic Metasurfaces. *Nat. Rev. Mater.* **2017**, *2*, 17010.

- (19) Butet, J.; Brevet, P.-F.; Martin, O. J. F. Optical Second Harmonic Generation in Plasmonic Nanostructures: From Fundamental Principles to Advanced Applications. *ACS Nano* **2015**, *9*, 10545–10562.

- (20) Liu, X.; Biswas, S.; Jarrett, J. W.; Poutina, E.; Urbas, A.; Knappenberger, K. L.; Vaia, R. A.; Nealey, P. F. Deterministic Construction of Plasmonic Heterostructures in Well-Organized Arrays for Nanophotonic Materials. *Adv. Mater.* **2015**, *27*, 7314–7319.

- (21) Chen, S.; Zeuner, F.; Weismann, M.; Reineke, B.; Li, G.; Valev, V. K.; Cheah, K. W.; Panoiu, N. C.; Zentgraf, T.; Zhang, S. Giant Nonlinear Optical Activity of Achiral Origin in Planar Metasurfaces with Quadratic and Cubic Nonlinearities. *Adv. Mater.* **2016**, *28*, 2992–2999.

- (22) Li, G.; Sartorello, G.; Chen, S.; Nicholls, L. H.; Li, K. F.; Zentgraf, T.; Zhang, S.; Zayats, A. V. Spin and Geometric Phase

Control Four-Wave Mixing from Metasurfaces. *Laser Photonics Rev.* **2018**, *12*, 1800034.

(23) Sun, M.; Zhang, Z.; Wang, P.; Li, Q.; Ma, F.; Xu, H. Remotely Excited Raman Optical Activity Using Chiral Plasmon Propagation in Ag Nanowires. *Light: Sci. Appl.* **2013**, *2*, No. e112.

(24) Roke, S.; Bonn, M.; Petukhov, A. V. Nonlinear Optical Scattering: The Concept of Effective Susceptibility. *Phys. Rev. B: Condens. Matter Mater. Phys.* **2004**, *70*, 115106.

(25) Steves, M. A.; Wang, Y.; Briggs, N.; Zhao, T.; El-Sherif, H.; Bersch, B. M.; Subramanian, S.; Dong, C.; Bowen, T.; Fuente Duran, A. D. L.; Nisi, K.; Lassauniere, M.; Wurstbauer, U.; Bassim, N. D.; Fonseca, J.; Robinson, J. T.; Crespi, V. H.; Robinson, J.; Knappenberger, K. L., Jr. Unexpected Near-Infrared to Visible Nonlinear Optical Properties from 2-D Polar Metals. *Nano Lett.* **2020**, *20*, 8312–8318.

(26) Johnson, C. J.; Dujardin, E.; Davis, S. A.; Murphy, C. J.; Mann, S. Growth and Form of Gold Nanorods Prepared by Seed-Mediated, Surfactant-Directed Synthesis. *J. Mater. Chem.* **2002**, *12*, 1765–1770.

(27) Streit, J. K.; Park, K.; Ku, Z.; Yi, Y.-J.; Vaia, R. A. Tuning Hierarchical Order and Plasmonic Coupling of Large-Area, Polymer-Grafted Gold Nanorod Assemblies via Flow-Coating. *ACS Appl. Mater. Interfaces* **2021**, *13*, 27445–27457.

(28) Park, K.; Hsiao, M.; Yi, Y.-J.; Izor, S.; Koerner, H.; Jawaid, A.; Vaia, R. A. Highly Concentrated Seed-Mediated Synthesis of Monodispersed Gold Nanorods. *ACS Appl. Mater. Interfaces* **2017**, *9*, 26363–26371.

(29) Zhou, X.; Andoy, N. M.; Liu, G.; Choudhary, E.; Han, K.-S.; Shen, H.; Chen, P. Quantitative Super-Resolution Imaging Uncovers Reactivity Patterns on Single Nanocatalysts. *Nat. Nanotechnol.* **2012**, *7*, 237–241.

(30) Nie, T.; Gong, X.-Q. Theoretical Study of Twinning Boundaries in Twinned Gold Nanorod Using Evolutionary Algorithms Aided Computational Simulations. *J. Phys. Chem. C* **2019**, *123*, 31103–31107.

(31) Schaefer, B.; Collett, E.; Smyth, R.; Barrett, D.; Fraher, B. Measuring the Stokes Polarization Parameters. *Am. J. Phys.* **2007**, *75*, 163–168.

(32) Park, K.; Yi, Y.-J.; Jawaid, A.; Busch, R.; Schantz, A. B.; Streit, J.; Izor, S.; Vaia, R. A. Toward an Alkahest Canopy for Gold Nanorod Stability in Water and Organic Solvents. *J. Phys. Chem. C* **2020**, *124*, 11730–11739.

(33) O'Brien, K.; Suchowski, H.; Rho, J.; Salandrino, A.; Kante, B.; Yin, X.; Zhang, X. Predicting Nonlinear Properties of Metamaterials from the Linear Response. *Nat. Mater.* **2015**, *14*, 379–383.

(34) Zhang, J.; Langille, M. R.; Mirkin, C. A. Synthesis of Silver Nanorods by Low Energy Excitation of Spherical Plasmonic Seeds. *Nano Lett.* **2011**, *11*, 2495–2498.